ACS NANO

www.acsnano.org

ARTICLE

Ordered DNA-Wrapped Single-Chirality Carbon Nanotubes Enable an Unparalleled Sensing Platform for Copper Ion Detection

Jianying Chen, Yinong Li, Jiajie Wu, Jialong Liu, Xuan Zhou, Zelong Li, Kunpeng Tang, Lei Shi, Zhilong Zhang, and Zhiwei Lin*

Cite This: *ACS Nano* 2025, 19, 28743−28754

Read Online

ACCESS | Metrics & More | Article Recommendations | Supporting Information

ABSTRACT: **Copper is an essential trace metal in living organisms, but excessive copper intake poses significant risks to plants, animals, and human health throughout the food chain. Developing a sensitive, nondestructive, and real-time technique to assess copper uptake in plants is highly desirable, yet it remains a challenging task. Here, we demonstrate that purified single-chirality carbon nanotubes (scCNTs) wrapped with a periodically ordered DNA structure provide an unparalleled platform for copper detection. By screening five distinct purified DNA-scCNT species, we identified $C_3GC_6GC_4$-(7,5) as the most promising candidate. It demonstrated ultrasensitive and highly selective detection of Cu^{2+} ions, with a limit of detection of 1.20 pM, and showed no interference from 13 competing ions. This system functions by efficiently adsorbing Cu^{2+} ions onto the surface of the (7,5) nanotubes through an ordered DNA wrapping structure. The electron transfer from (7,5) to Cu^{2+} significantly quenches the nanotube fluorescence. Femtosecond transient absorption (fs-TA) measurements revealed that the electron transfer occurs on a femtosecond time scale. $C_3GC_6GC_4$-(7,5) was successfully applied as a nanosensor for real-time, rapid, and quantitative detection of Cu^{2+} uptake in living plants. Our findings highlight the superiority of purified DNA-scCNT sensors, establishing a paradigm for next-generation nanosensors.**

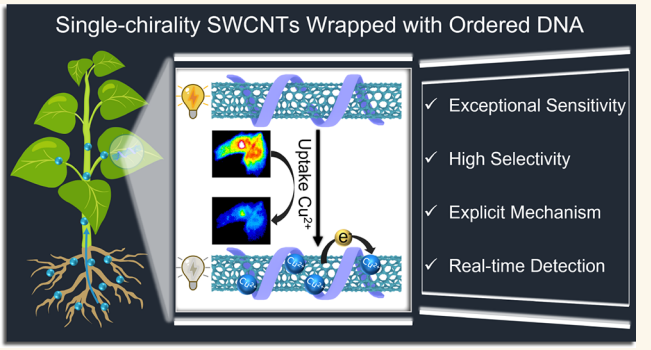

KEYWORDS: *single-chirality carbon nanotubes, ordered DNA structures, electron transfer, ion detection, photoluminescence*

INTRODUCTION

Copper is one of the essential trace metallic elements necessary for the normal functioning of the central nervous system and immune system, as well as for the growth and development of internal organs and the activity of various enzymes.[1] However, with the rapid development of industry and the widespread use of copper-containing pesticides, the problem of copper pollution in the environment is becoming increasingly severe.[2] This excessive copper pollution has exceeded the tolerance range of the ecosystem, posing threats not only to plants, animals, and soil microorganisms but also having a deleterious impact on human health through the food chain.[3,4] Excessive long-term intake of copper will damage the kidneys and liver, cause abnormalities in the blood−brain barrier function, and potentially lead to Alzheimer's disease.[5,6]

It has been reported that approximately 40−45% of the dietary copper intake comes from vegetables and plant-based sources.[7] The conventional method for determining copper levels in plants and soil, which relies on mass spectrometry, involves field sampling, followed by the digestion and extraction of plant tissues.[8−10] This process demands substantial labor for sample pretreatment and expensive instrumentation. Moreover, it does not enable real-time monitoring of copper contamination in the field. Therefore, it is highly desirable but challenging to develop a facile and sensitive technique that can assess copper uptake in plants in real time and determine the concentration of copper in agricultural soil.

Single-walled carbon nanotubes (CNTs) have found extensive applications in biological sensing and imaging technologies due to their fluorescence in the near-infrared

Received: May 20, 2025
Revised: July 21, 2025
Accepted: July 22, 2025
Published: August 1, 2025

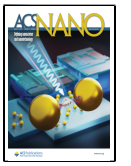

https://doi.org/10.1021/acsnano.5c08364
ACS Nano 2025, 19, 28743−28754

(NIR) region.[11−17] Unless otherwise stated, CNTs in this work refer to single-walled carbon nanotubes. The wrapping of DNA on CNTs,[18] known as DNA-CNTs, not only confers water solubility and biocompatibility to the nanotubes[19] but also expands their utility in diverse fields ranging from disease diagnosis to agricultural biotechnology.[20−24] DNA-CNTs have garnered tremendous attention as a promising sensing platform due to several key factors: (i) their sensitive fluorescence response to changes in the local environment,[25−28] (ii) the versatility enabled by the unlimited combination of DNA sequences and CNT chirality types,[29−34] and (iii) their ease of preparation and high stability.[35−37] Despite significant advancements in DNA-CNT sensors, the widely utilized variety remains unpurified CNTs with a mix of chiralities (Figure 1a). Their sensing performance is severely compromised by the presence of metallic CNTs, which could potentially quench the fluorescence of sensors,[11,38] as well as various semiconducting tubes that cause spectral congestion.[39,40] Furthermore, the compositional heterogeneities and ill-defined DNA structures present in the unpurified sensors have significantly impeded our understanding of the sensing mechanisms.[41−43]

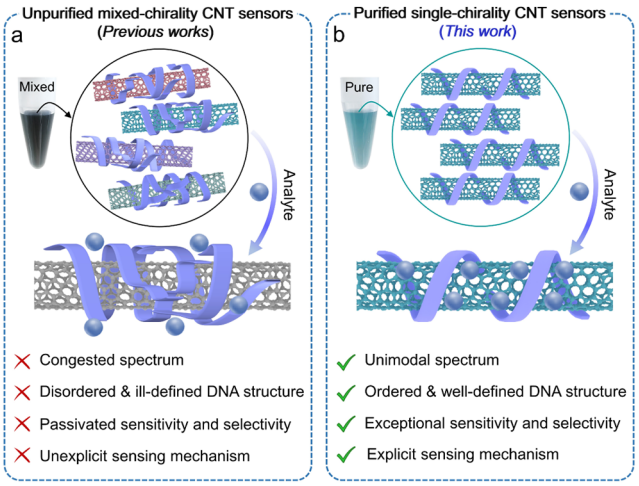

Figure 1. Comparison of unpurified and purified DNA-CNT sensors. Structural and sensing properties of (a) unpurified mixed-chirality CNTs with an ill-defined DNA structure and (b) purified scCNTs with a well-defined DNA structure.

Herein, we report an ultrasensitive platform for real-time detection of copper using purified single-chirality CNTs (scCNTs), which are wrapped by DNA with a periodically ordered structure (Figure 1b). By screening five distinct purified DNA-scCNT species, we identified the $C_3GC_6GC_4$-(7,5) species as the most promising candidate, exhibiting exceptional sensitivity, selectivity, and stability in detecting Cu^{2+} ions. This can be attributed to both the chirality type of (7,5) and the ordered DNA wrapping structures. Additionally, the purified $C_3GC_6GC_4$-(7,5) exhibited superior Cu^{2+} sensing capabilities compared to its unpurified (7,5) counterpart or purified (7,5) coated with disordered DNA. The purified DNA-scCNT sensors enabled us to explicitly elucidate the sensing mechanism, which is challenging to achieve using mixed-chirality sensors. We confirmed that the complexation with DNA brings Cu^{2+} ions into close proximity to the surface of CNTs, and the electron transfer from (7,5) to Cu^{2+} resulted in the fluorescence quenching of nanotubes. Femtosecond transient absorption (fs-TA) experiments suggested that the electron transfer took place on a femtosecond time scale and accelerated the relaxation of photogenerated electrons in the excited state. Benefiting from the exceptional sensing capabilities of $C_3GC_6GC_4$-(7,5), they were utilized as an NIR fluorescent nanosensor for Cu^{2+} detection in living plants. The ultrasensitive response to Cu^{2+} in vivo has enabled rapid, real-time, and nondestructive NIR fluorescent imaging of Cu^{2+} uptake from plant roots.

RESULTS AND DISCUSSION

Screening of Purified DNA-scCNTs. To obtain purified sensors, we utilized the aqueous two-phase (ATP) technique to separate five distinct types of scCNTs by using their respective resolving DNA sequences. Each resolving sequence forms unique ordered wrapping structures on its target scCNTs while creating disordered structures on nontarget CNTs.[41] The ordered DNA conformation, stabilized by hydrogen bonding networks,[41] minimizes structural variation and conformational entropy, distinguishing it from disordered DNA-CNT structures and facilitating nanotube separation in the ATP system.[32] The protocol for ATP separation is delineated in the Supporting Information. The purified DNA-scCNT species include $(GCC)_2(CCG)_2$-(6,4), $C_3(CCG)_3$-(9,1), $T_3C_3T_3C_6$-(8,3), $TTA(TAT)_2ATT$-(6,5), and $C_3GC_6GC_4$-(7,5), whose chirality and purity were confirmed by UV−vis−NIR absorption and photoluminescence (PL) spectra (Figure S1). The main E_{11} emission peaks of the five scCNTs are centered at 890, 928, 968, 993, and 1038 nm, respectively. In addition to the main PL peaks, the presence of minor peaks at 1050 nm for (6,4), 1092 nm for (9,1), 1134 nm for (8,3), and 1206 nm for (7,5) can be attributed to the charged excitons (i.e., trions).[44] These peaks fall within the NIR fluorescence emission spectrum, which is considered as the ideal spectral window for biomedical imaging due to its ability to penetrate deep into tissue without significant absorption or scattering.[11] We have recently reported that resolving sequences construct periodically helical structures on their target scCNTs with distinct pitches, and the resulting DNA-scCNTs exhibited pitch-dependent sensing performance in neurotransmitter detection.[41] We hypothesize that these purified DNA-scCNT sensors may display diverse sensing capabilities for ion detection, as the interactions between ions and DNA molecules are largely influenced by the specific DNA sequences and their hierarchical structures.[45,46]

The optical response of purified DNA-scCNT sensors to Cu^{2+} ions was initially examined by exposing them to a solution of 10^{-8} M Cu^{2+}. The response is highly dependent on the chirality type of the nanotube. Figure 2a,b shows the typical PL spectra of $C_3GC_6GC_4$-(7,5) and $TTA(TAT)_2ATT$-(6,5) before and after the introduction of Cu^{2+} ions. Hereafter, we denote $C_3GC_6GC_4$-(7,5) as (7,5) for simplicity, a notation that is also applicable to other DNA-scCNTs. The spectral responses for the other three DNA-scCNTs can be found in Figure S2. It is evident that (9,1), (8,3), and (7,5) demonstrated an obvious decrease in PL intensity upon exposure to Cu^{2+} ions, whereas (6,4) and (6,5) exhibited a negligible optical response. The sensitivity (S) of the optical response can be quantified using the expression $S = (I - I_0)/I_0$, where I_0 and I represent the PL intensity before and after the addition of Cu^{2+} ions, respectively. The most pronounced PL change was observed for (7,5) with an S value of −0.5 (Figure 2c), followed by (8,3) and (9,1), which exhibited S values of

https://doi.org/10.1021/acsnano.5c08364
ACS Nano 2025, 19, 28743−28754

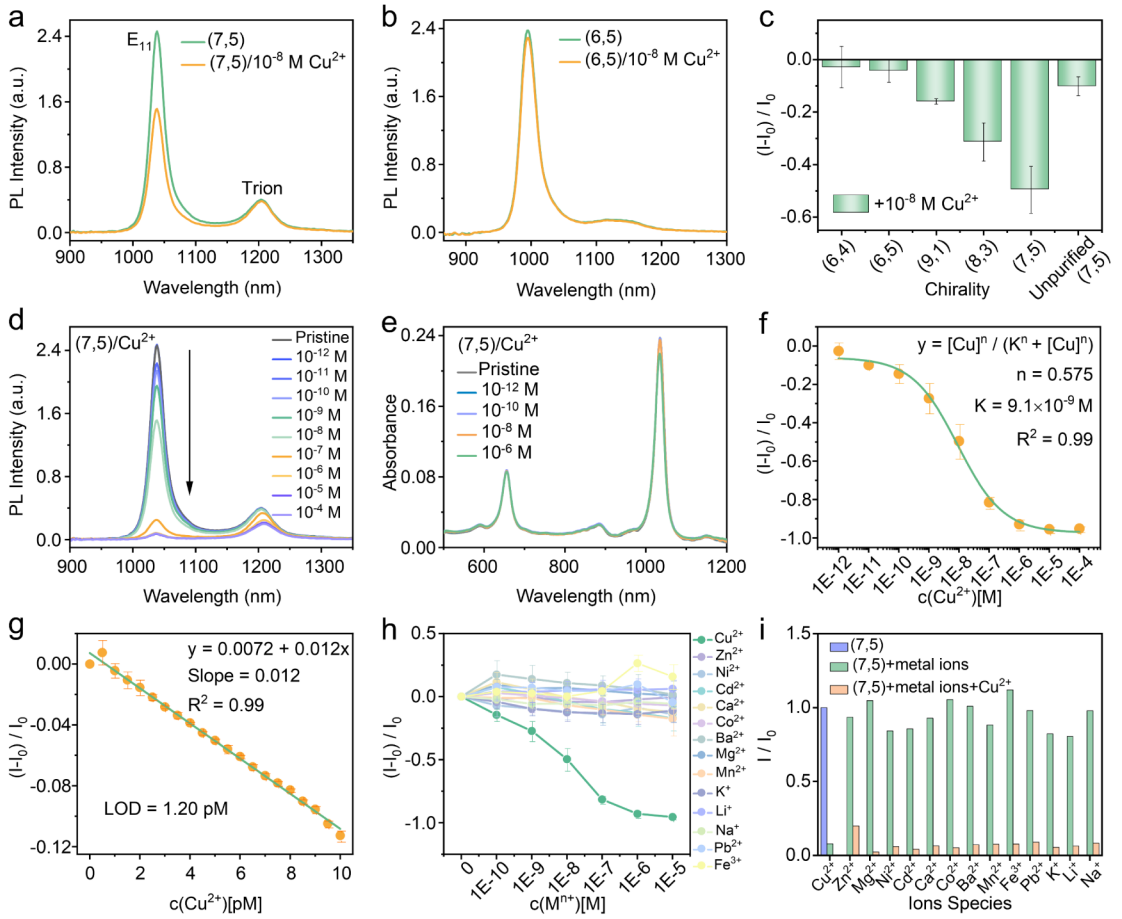

Figure 2. Sensing performance of purified DNA-scCNTs toward Cu^{2+} ions. (a, b) PL spectra of $C_3GC_6GC_4$-(7,5) and $TTA(TAT)_2ATT$-(6,5) before and after the addition of 10^{-8} M Cu^{2+}. (c) Sensitivity of five distinct types of purified DNA-scCNTs and unpurified (7,5) in the detection of Cu^{2+}. All types of DNA-CNTs were prepared to an identical concentration (optical density, OD = 0.2) for sensitivity measurement. (d) PL and (e) absorption spectra of (7,5) upon the addition of varying concentrations of Cu^{2+}. (f) Response curve of (7,5) toward Cu^{2+}, with the data points fitted by the Hill equation. (g) Response of (7,5) toward Cu^{2+} at low concentrations, with the data points fitted by a linear equation. (h) Response of (7,5) toward various metal ions. (i) Response of (7,5) toward Cu^{2+} (10^{-6} M) in the copresence of other metal ions (10^{-6} M). The data are represented as the mean ± standard deviation derived from 3 independent experiments.

−0.3 and −0.15, respectively. The underlying mechanism of chirality-dependent sensitivity will be discussed in a later section.

To make a direct comparison between purified and nonpurified CNTs, we subsequently investigated the optical response of unpurified DNA-CNT dispersions to Cu^{2+} ions. The dispersions were prepared by using commercial SG65i CNTs, which were dispersed by various DNA sequences. Figure S3a shows a typical PL spectral variation of the $C_3GC_6GC_4$−CNT dispersion before and after the addition of 10^{-8} M Cu^{2+} ions. As anticipated, an optical response was observed across multiple wavelengths concurrently. These unpurified DNA-CNTs exhibited a featureless decrease in their PL intensity when exposed to Cu^{2+}, regardless of the DNA sequences (Figure S3b−d). Due to the overlapping of spectral peaks, it was difficult to quantify the sensitivity of each chirality. We deconvoluted the response of (7,5) in the unpurified DNA-CNT dispersion and calculated an S value of −0.1 (Figure 2c). Both purified and unpurified (7,5) were wrapped with the same $C_3GC_6GC_4$; however, purified (7,5) exhibited a significantly higher sensitivity (S = −0.5) to Cu^{2+} compared to the unpurified one (S = −0.1). This discrepancy can be attributed to the spectral congestion and the presence of metallic tubes in the unpurified dispersion, as previously discussed. We reiterate that these issues substantially compromise the detection capabilities of DNA-CNT sensors, thereby reinforcing the significance of developing purified scCNT sensors.

Sensing Performance of Purified $C_3GC_6GC_4$-(7,5) toward Cu^{2+} Ions. Due to the high sensitivity of the purified (7,5) toward Cu^{2+} ions, it was chosen as the standard sensor for comprehensive investigation. Figure 2d shows the PL spectra of (7,5) in response to varying concentrations of Cu^{2+} ions, spanning from 10^{-12} to 10^{-4} M. The PL intensity dramatically decreased with increasing Cu^{2+} concentration, with the emission of (7,5) being reduced by 90% at 10^{-6} M or higher. The optical response of (7,5) to Cu^{2+} was investigated in the presence of various anions, including NO_3^-, SO_4^{2-}, and Cl^-, indicating that its sensitivity is anion-independent (Figure S4). Furthermore, (7,5) exhibited stable emission spectra under various conditions, including incubation at temperatures up to 60 °C for 1 h, at ambient temperature for 15 days (Figure S5), or across a pH range of 4 to 10 (Figure S6). Notably, the (7,5) sensors retained a sensitive fluorescence response to Cu^{2+} ions throughout the pH range of 5 to 9 (Figure S7), which corresponds to the typical pH values found

https://doi.org/10.1021/acsnano.5c08364
ACS Nano 2025, 19, 28743−28754

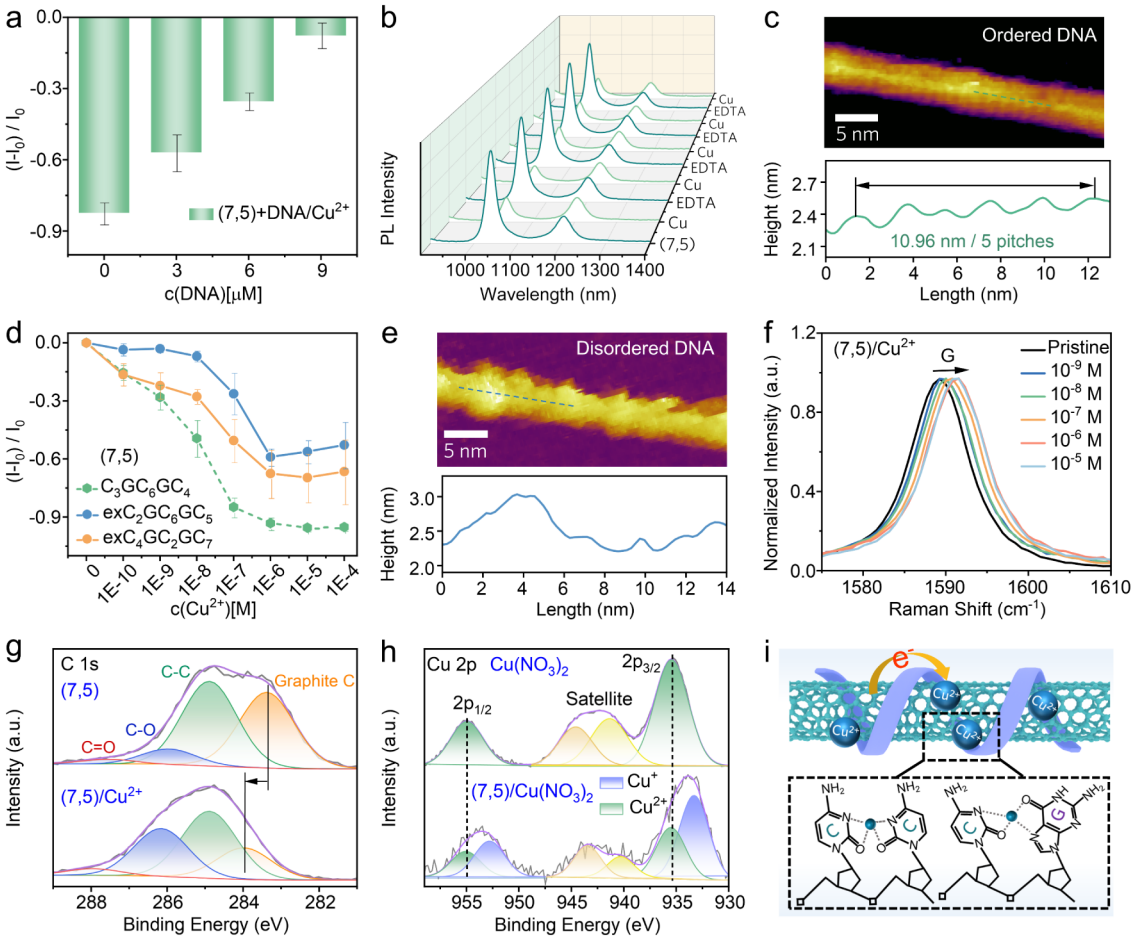

Figure 3. Sensing mechanism of $C_3GC_6GC_4$-(7,5) toward Cu^{2+} ions. (a) PL response of (7,5) toward 10^{-7} M Cu^{2+} in the presence of different concentrations of additional free DNA. (b) PL spectra of (7,5) upon the alternating addition of Cu^{2+} (10^{-6} M) and EDTA (10^{-6} M). (c) High-resolution AFM height image of (7,5) wrapped with ordered $C_3GC_6GC_4$ and the corresponding height profile measurement along the nanotube. The average helical pitch of DNA can be obtained from direct measurement. (d) PL response of (7,5) coated with nonresolving DNA sequences toward Cu^{2+}. The response of $C_3GC_6GC_4$-(7,5) is illustrated by the dashed line for comparative purposes. (e) High-resolution AFM height image of (7,5) coated with a nonresolving sequence ($C_2GC_6GC_5$) and the corresponding height profile measurement along the nanotube. (f) Magnified regions of the G peaks in the Raman spectra of (7,5) upon the addition of varying Cu^{2+} concentrations. (g) C 1s XPS spectra of (7,5) before and after the addition of Cu^{2+}. (h) Cu 2p XPS spectra of $Cu(NO_3)_2$ before and after chelating with (7,5). (i) Schematic diagram illustrating the interaction between Cu^{2+} ions and the (7,5) wrapped with ordered DNA, highlighting the mechanism of Cu^{2+} detection by DNA-CNTs.

in most biological tissues. This signifies that (7,5) sensors are suitable for in vivo Cu^{2+} detection applications, *vide infra*. It is worth noting that despite a significant decrease in the PL intensity of (7,5) upon Cu^{2+} addition, the corresponding absorption remains stable (Figure 2e). This implies that the reduction in PL intensity is not due to nanotube aggregation but instead a result of nanotube fluorescence quenching by Cu^{2+} ions.

The responses of (7,5) against different concentrations of Cu^{2+} ions could be well fitted by the Hill equation $Y = \frac{X^n}{K^n + X^n}$, where Y is the normalized response, X is the analyte concentration, n is the Hill coefficient, and K is the dissociation constant. The analysis yielded a K value of 9.1×10^{-9} M and an n value of 0.575 (Figure 2f). For comparison, the response of unpurified (7,5) sensors in dispersion was also fitted by the Hill equation (Figure S8), giving a K value of 2.1×10^{-7} M and an n value of 1.06. The unpurified (7,5) exhibited a much bigger K value than the purified one, indicating a weaker binding affinity toward Cu^{2+} ions.[47] This may be attributed to the competitive binding from various chiralities of DNA-CNTs within the unpurified system, which necessitates a higher concentration of Cu^{2+} to achieve half occupation of the binding sites on DNA-CNTs. The difference in K values also explains the lower sensitivity of unpurified (7,5) compared to the purified counterparts (Figure 2c). The limit of detection (LOD) of the purified (7,5) was determined to be as low as 1.20 pM (Figures 2g and S9), demonstrating its ultrasensitive ability to detect Cu^{2+} ions—over 3 orders of magnitude more sensitive than existing methods.[48−50]

We next investigated the selectivity of the (7,5) sensors toward Cu^{2+} by examining their optical response to a range of metal ions commonly found in biological systems, including Zn^{2+}, Ni^{2+}, Cd^{2+}, Ca^{2+}, Co^{2+}, Ba^{2+}, Mg^{2+}, Mn^{2+}, K^+, Li^+, Na^+, Pb^{2+}, and Fe^{3+}. In contrast to Cu^{2+}, these metal ions exerted a minor effect on the PL intensity of (7,5) at the tested concentration, ranging from 10^{-10} to 10^{-5} M (Figures 2h and S10). Anti-interference ability is an important criterion for evaluating the specificity of optical sensors in practical applications. To assess this attribute, we detected Cu^{2+} in the

https://doi.org/10.1021/acsnano.5c08364
ACS Nano 2025, 19, 28743−28754

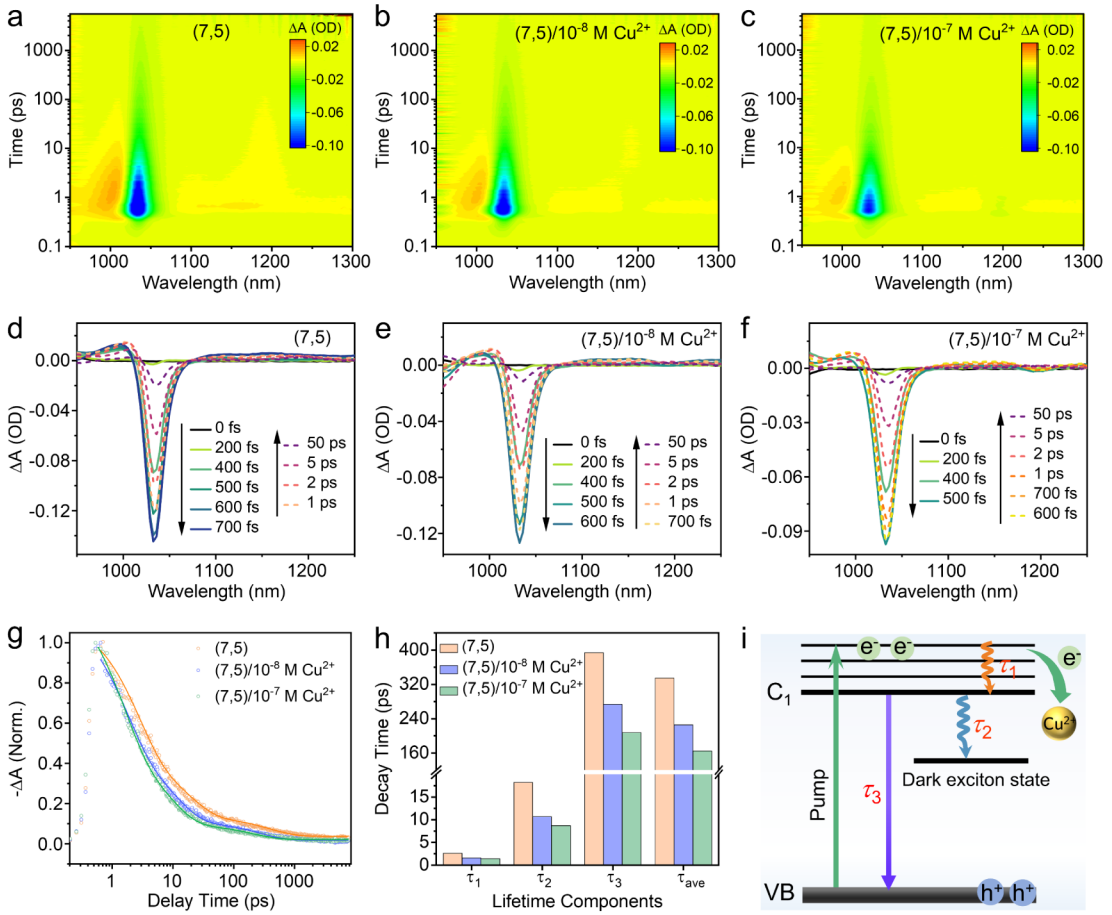

Figure 4. Femtosecond transient absorption spectroscopy of (7,5) in the absence and presence of Cu^{2+} ions. (a) 2D fs-TA map and (d) early time (0 fs to 50 ps) fs-TA spectra for (7,5). (b) 2D fs-TA map and (e) early time (0 fs to 50 ps) fs-TA spectra for (7,5)/10^{-8} M Cu^{2+}. (c) 2D fs-TA map and (f) early time (0 fs to 50 ps) fs-TA spectra for (7,5)/10^{-7} M Cu^{2+}. (g) Fitted GSB decay kinetics for (7,5) and (7,5)/Cu^{2+}. (h) Lifetimes of three excited decay pathways for (7,5) and (7,5)/Cu^{2+}. (i) Schematic diagram illustrating the excited-state relaxation dynamics of (7,5) and electron transfer with Cu^{2+}. All fs-TA measurements were excited by a 900 nm pump pulse.

copresence of other metal ions (10^{-6} M) and observed that these metal ions did not interfere with the detection of Cu^{2+} by (7,5), demonstrating an exceptional anti-interference ability (Figure 2i).

Sensing Mechanism of $C_3GC_6GC_4$-(7,5) toward Cu^{2+} Ions. The above results underscore that $C_3GC_6GC_4$-(7,5) is an ultrasensitive, selective, and robust sensor for the detection of Cu^{2+} ions. To elucidate the sensing mechanism, we investigated the interaction between $C_3GC_6GC_4$-(7,5) and Cu^{2+} ions. It has been reported that Cu^{2+} ions can bind to DNA with high affinity.[45] We assessed the interaction between Cu^{2+} and free $C_3GC_6GC_4$ DNA using Fourier Transform Infrared (FTIR) spectroscopy. As shown in Figure S11b,c, the bands at 1517 cm^{-1}, 1555 cm^{-1}, and 1566 cm^{-1}, corresponding to the complexation of cytosine (*N*-3 position) and guanine (*N*-7 position) with Cu^{2+}, gradually appeared as the Cu^{2+} concentrations increased. Additionally, the bands associated with the nucleic acid bases at 1503 cm^{-1} and 1580 cm^{-1} shifted to 1507 cm^{-1} and 1583 cm^{-1}, respectively. Concurrently, stretching vibrations at 1648 cm^{-1} (C_2=O of cytosine) and 1680 cm^{-1} (C_6=O of guanine) gradually increased, while the bands corresponding to the phosphate backbone remained unchanged (Figure S11a). This suggests that Cu^{2+} ions primarily bind to the *N*-7 position and C_6=O of guanine as well as the *N*-3 position and C_2=O of cytosine within the $C_3GC_6GC_4$ molecules.[45,51]

To explore the DNA−Cu^{2+} interaction further within a sensing framework, we incorporated additional $C_3GC_6GC_4$ into the $C_3GC_6GC_4$-(7,5) sensing system and evaluated its Cu^{2+} detection ability (Figures 3a and S13). A significant reduction in sensitivity was detected as the concentration of free DNA increased. Based on these observations, we propose that upon the introduction of Cu^{2+} ions into $C_3GC_6GC_4$-(7,5), they are bound by DNA wrapping around the (7,5), thereby bringing them into proximity to the surface of the nanotube. The interplay between Cu^{2+} ions and (7,5) nanotubes led to the suppression of fluorescence emission. To further validate the hypothesis, ethylenediaminetetraacetic acid (EDTA), a potent chelating agent for Cu^{2+}, was introduced into the $C_3GC_6GC_4$-(7,5) sensing system, which already contained 10^{-6} M Cu^{2+}. The quenched fluorescence was promptly and fully recovered (Figure 3b). Since EDTA has a much stronger affinity for Cu^{2+} ions than DNA, the chelation of Cu^{2+} ions with EDTA prevents their interaction with (7,5) nanotubes, leading to the recovery of fluorescence. Notably, the processes of fluorescence quenching and recovery can be repeated for multiple cycles without adversely affecting the sensing performance (Figure S14).

https://doi.org/10.1021/acsnano.5c08364
ACS Nano 2025, 19, 28743−28754

Figure 3c presents a high-resolution atomic force microscopy (AFM) image of $C_3GC_6GC_4$-(7,5), which was measured using a protocol we recently developed.[41] $C_3GC_6GC_4$ creates an ordered wrapping structure around the (7,5) nanotube, consistent with our earlier findings on other purified DNA-scCNTs. The reversible sensing behaviors imply that Cu^{2+} ions do not disrupt the ordered wrapping structure of $C_3GC_6GC_4$. The helical pitch of $C_3GC_6GC_4$ was measured to be ~ 2.2 nm, which is larger than that observed for other purified DNA-scCNTs, whose pitches were reported in our previous work.[41] A larger pitch provides more open space to accommodate Cu^{2+} ions, which partly accounts for the superior sensitivity of (7,5) compared to other purified nanotubes (an additional interpretation will be discussed in the following paragraph). Notably, the purified (7,5) nanotubes coated with non-resolving sequences via DNA−DNA exchange[52] exhibited significantly reduced sensing capability (Figure 3d). This is because the nonresolving sequences form disordered and thicker coating structures on (7,5) (Figure 3e). Additional AFM images and discussions of the ordered and disordered structures of DNA can be found in Figure S15. As illustrated in Figure 1a, the disordered structures prevent Cu^{2+} ions from approaching the surface of the (7,5) nanotubes, thereby reducing the efficacy of fluorescence quenching. These findings emphasize that the ordered DNA conformation is crucial for ensuring the excellent sensing capabilities of $C_3GC_6GC_4$-(7,5).

To explore the molecular mechanism underlying the fluorescence quenching of (7,5) by Cu^{2+}, we conducted a series of experiments. First, Raman spectroscopy was utilized to investigate the electronic state changes of the nanotubes (Figure S16a). Both the G band and the G′ band experienced a shift to a higher frequency as the Cu^{2+} concentration increased (Figures 3f and S16a−d). This upshift indicates the transfer of electrons out of the nanotubes.[53−58] In contrast, the G bands remained unaffected when (7,5) was exposed to other divalent metal ions, such as Mg^{2+}, Zn^{2+}, and Cd^{2+} (Figure S16e,f). This is consistent with the observation that (7,5) was insensitive to these ions, as presented in Figure 2h. Second, high-resolution X-ray photoelectron spectroscopy (XPS) was performed to analyze the surface chemical state of (7,5) sensors. Figure 3g shows the C 1s XPS spectra for (7,5) before and after the introduction of Cu^{2+}. The peak located at ~283.4 eV is assigned to graphitic carbons on the pristine nanotubes. Upon the addition of Cu^{2+}, the binding energy of these carbons increases to around 283.9 eV, signifying electron loss from the nanotubes.[59,60] Meanwhile, the appearance of additional peaks corresponding to Cu^{+} in the XPS spectra of (7,5)/Cu^{2+} indicates electron gain by Cu^{2+} (Figures 3h and S17).[61,62] These findings reveal that fluorescence quenching is a result of nanotube oxidation, with electrons being transferred from nanotubes to Cu^{2+} (Figure 3i). Since the reduction potentials of nanotubes are inversely proportional to their diameters, the (7,5) nanotube, with the biggest diameter among the five types of nanotubes studied, is the most susceptible to oxidation.[63−65] This further explains its higher sensitivity to Cu^{2+} compared with other types of purified DNA-scCNTs.

Exciton Dynamics in Electron Transfer from (7,5) to Cu^{2+} Ions. To gain further insight into the sensing mechanism, femtosecond transient absorption (fs-TA) spectroscopy was used to study the excited-state relaxation dynamics of (7,5) and electron transfer to Cu^{2+}. As shown in Figure 4a,d, the fs-TA spectra of (7,5) exhibited a pronounced negative peak at 1035 nm and a positive peak (900−1020 nm) in the change of absorbance (ΔA) upon excitation with a pump pulse of 900 nm. These two peaks were assigned to ground-state bleach (GSB) and excited-state absorption (ESA), respectively.[66,67] The GSB peak of (7,5) mainly reflects the excited-state relaxation, which involves the generation and subsequent relaxation of photogenerated electrons. Upon excitation, the GSB peak quickly reaches a maximum at 700 fs, indicating the generation and filling of electrons in the conduction band.[67,68] Subsequently, the intensity of the GSB peak decreases rapidly within 50 ps (Figure 4d) and then decays more slowly on an extended time scale. Upon the addition of Cu^{2+}, the GSB signal reaches a maximum more quickly, manifested as the GSB peak achieving its maximum within 600 and 500 fs in the presence of 10^{-8} M and 10^{-7} M Cu^{2+}, respectively (Figure 4b,c,e,f). The accelerated electron filling observed upon the addition of Cu^{2+} suggests that the electron transfer from (7,5) to Cu^{2+} occurs on a femtosecond time scale during the electron filling process. Meanwhile, the ESA signal of (7,5)/Cu^{2+} was suppressed in comparison with (7,5), further validating the decrease of excited electrons due to the transfer (Figure S19).

To quantitatively elucidate the kinetics in the excited state, we fit the GSB decay curves of (7,5) and (7,5)/Cu^{2+} as shown in Figure 4g by the following triple exponential function:[68]

$$y = y_0 + A_1\exp\left(-\frac{t}{\tau_1}\right) + A_2\exp\left(-\frac{t}{\tau_2}\right) + A_3\exp\left(-\frac{t}{\tau_3}\right)$$

where A_x (x = 1, 2, 3) is the percentage of charge carriers involved in each process, and τ_x (x = 1, 2, 3) represents the corresponding lifetimes of the charge carriers. The average lifetime (τ_{ave}) can be calculated using the following equation:[68]

$$\tau_{ave} = \frac{A_1 \times \tau_1^2 + A_2 \times \tau_2^2 + A_3 \times \tau_3^2}{A_1 \times \tau_1 + A_2 \times \tau_2 + A_3 \times \tau_3}$$

The fitting results revealed that three lifetimes of (7,5) were 2.6, 18.2, and 393.7 ps, respectively. The τ_{ave} value was calculated to be 335 ps. These three lifetimes correspond to three distinct decay pathways that govern the relaxation of photogenerated electrons in the excited state. According to previous studies, we suggest that the short lifetimes, τ_1 and τ_2, are attributed to intraband exciton relaxation[69,70] and elastic defect scattering of charge carriers into the dark exciton state,[71] respectively. The long lifetime, τ_3, is ascribed to the radiative recombination of electrons and holes.[67] Upon the addition of Cu^{2+}, the three lifetimes were shortened and exhibited an inverse relationship with the Cu^{2+} concentration (Figure 4g,h). At concentrations of 10^{-8} and 10^{-7} M Cu^{2+}, the lifetimes decreased to τ_1 = 1.6 ps, τ_2 = 10.7 ps, τ_3 = 273.5 ps, and τ_1 = 1.4 ps, τ_2 = 8.8 ps, and τ_3 = 207.5 ps, with τ_{ave} values of 230.8 and 164.5 ps (Table S2), respectively. These results indicate that electron transfer may occur throughout the entire de-excitation process, thereby reducing the population of electrons that would otherwise be released via intraband exciton relaxation (τ_1), charge carrier scattering into the dark exciton state (τ_2), and exciton recombination (τ_3) (Figure 4i). Increasing the concentration of Cu^{2+} enhances the chance of (7,5) nanotubes interacting with Cu^{2+}, thereby accelerating the electron transfer rate and reducing the excited electron lifetime in the nanotubes. This aligns with observations in other donor−acceptor systems with similar charge transfer mechanisms,[72,73] where the excited electron lifetime is inversely proportional to the acceptor concentration.

https://doi.org/10.1021/acsnano.5c08364
ACS Nano 2025, 19, 28743−28754

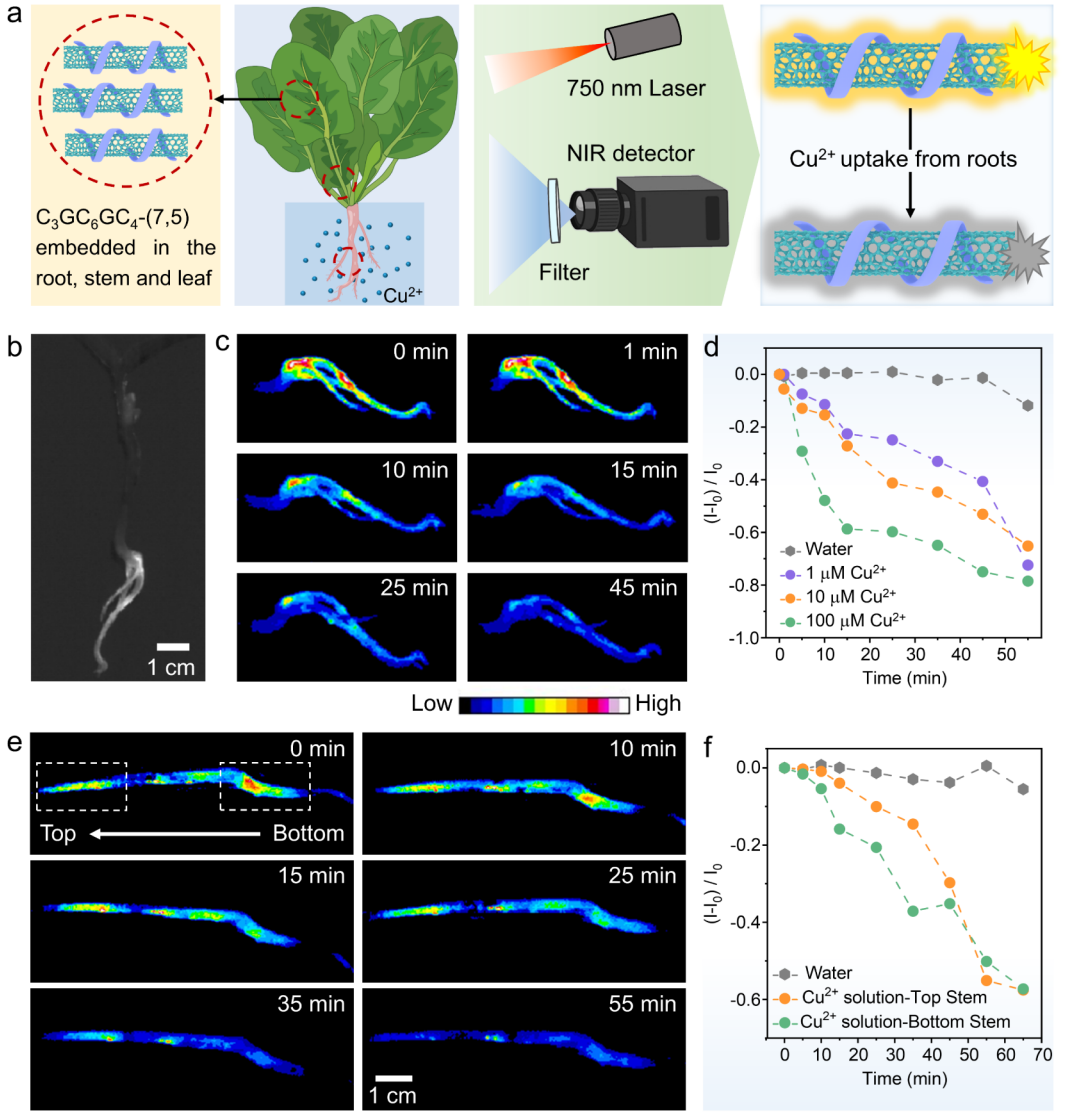

Figure 5. Detection of Cu^{2+} in living plants. (a) Schematic representation of the (7,5) sensor for real-time detection of Cu^{2+} in plants using an NIR camera and a 750 nm laser. (b) Bright-field image of a bean seedling treated with (7,5). (c) False-colored images illustrating the time-dependent fluorescence changes in the roots of a bean seedling cultured in a 10 μM Cu^{2+} solution. (d) Fluorescence intensity changes in the roots of bean seedlings cultured in water and various concentrations of Cu^{2+} solution. (e) False-colored images illustrating the time-dependent fluorescence changes in the stem of a bean seedling cultured in a 10 μM Cu^{2+} solution. (f) Fluorescence intensity changes in the stem of a bean seedling cultured in water and 10 μM Cu^{2+} solution.

Real-Time Imaging and Detection of Cu^{2+} Uptake in Living Plants. The highly sensitive and selective sensing capabilities of (7,5) toward Cu^{2+} render it a promising nano-optical sensor for real-time detection of Cu^{2+} in plants. This can be achieved by detecting the fluorescence change of embedded (7,5) in response to the uptake of Cu^{2+} ions from the plant's roots (Figure 5a). The experiment was facilitated by an integrated NIR imaging system, which incorporates a 750 nm laser and an InGaAs detector (Figure S21). Due to their nanosized and biocompatible nature, DNA-CNTs are expected to be readily absorbed by plants without adversely affecting their growth.[74,75] We first demonstrate the absorption of our nanosensors in live plants by culturing bean seedlings in a dilute solution of (7,5) and monitoring the real-time fluorescence of the plants (Figure S22). The fluorescence intensity gradually increased over time, indicating that the nanotubes were transported into the plants. The nanotubes began to be absorbed by the root of bean seedlings within 10 min and reached saturation after 100 min (Figure S23). The NIR fluorescence of absorbed nanotubes exhibited high photostability, showing no signs of photobleaching and remaining unaffected by chlorophyll autofluorescence. These characteristics further enhance the advantages of DNA-scCNT sensors for sensing applications in plants.

To effectively monitor the distribution and concentration changes of Cu^{2+} ions within plants in real time, (7,5) sensors were integrated into different parts of the plants, including the roots, stems, and leaves. First, to investigate the capabilities of absorbed (7,5) to detect Cu^{2+} within the roots, we selected bean seedlings with a simple root and stem system as our model plants. The seedlings were initially cultured in a diluted (7,5) solution for 2 h to obtain a clear NIR signal (Figure 5b), followed by transferring them into a solution of Cu^{2+} ions (Figure S24). The Cu^{2+} concentration used in the plant imaging study is in the micromolar range, which is typical for hydroponic nutrient solutions for vegetables.[76] Over time, the

https://doi.org/10.1021/acsnano.5c08364
ACS Nano 2025, 19, 28743−28754

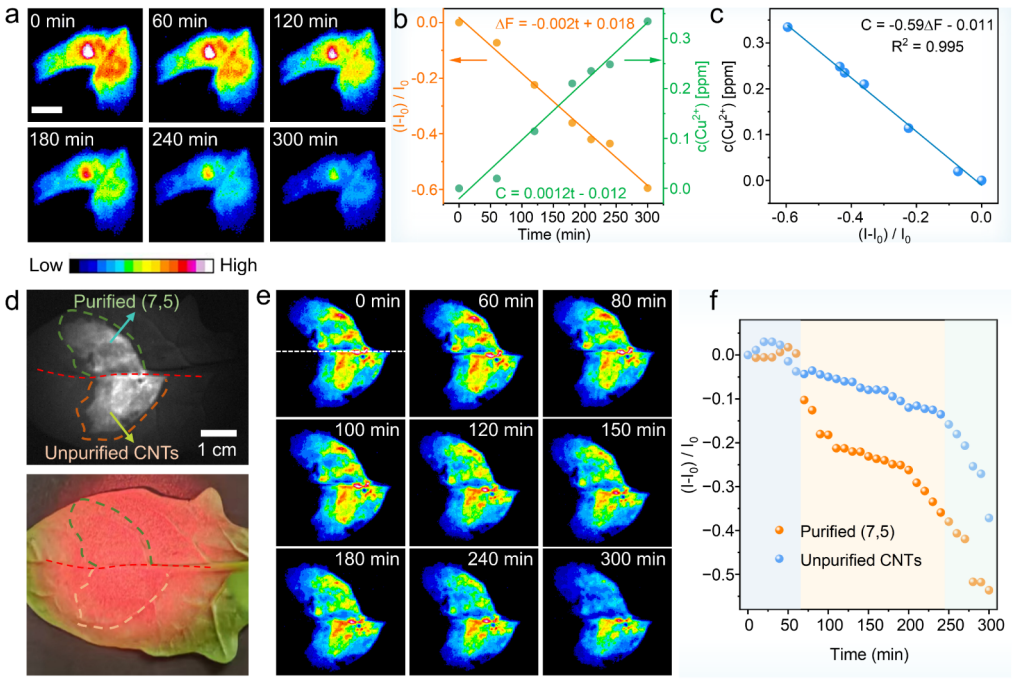

Figure 6. Real-time detection of Cu^{2+} in spinach leaves. (a) False-colored fluorescence images and (b) time-dependent fluorescence intensity changes (orange line) of the spinach leaf upon the addition of a 10 μM Cu^{2+} solution into the root environment. The green line represents the linear fit of the Cu^{2+} accumulation in the leaves, as measured by ICP. (c) Linear fit of the fluorescence change and the accumulated Cu^{2+} levels in the leaves, as measured by ICP. (d) Bright-field image and photograph of a spinach leaf infiltrated with both purified (7,5) and unpurified CNTs. (e) False-colored fluorescence images and (f) time-dependent fluorescence intensity changes of the spinach leaf upon the addition of a 10 μM Cu^{2+} solution to the root environment.

fluorescence intensity of bean seedlings progressively decreased as Cu^{2+} was absorbed and transported from the roots into the vascular bundle (Figure 5c). Within 45 min of exposure to a 10 μM Cu^{2+} solution, the fluorescence intensity decreased by approximately 53%. The reduction in fluorescence intensity was proportional to the concentration of Cu^{2+} ions in the culture medium during the first hour of exposure, until the Cu^{2+} ions reached a superaccumulated level in the roots (Figure 5d). As a control, no reduction in fluorescence was detected when the plant was nourished in deionized water for 180 min (Figures S25 and S26). These observations indicate that (7,5) maintains its capabilities in detecting and tracing Cu^{2+} within biological systems.

Next, we focused on monitoring the transport of Cu^{2+} within the stem. To this end, we injected (7,5) into the stem of the bean seedling, which was subsequently cultured in a 10 μM Cu^{2+} solution. As shown in Figure 5e,f, the fluorescence intensity at the bottom of the stem diminished noticeably within the initial 15 min, as a consequence of the plant's transpiration process. In contrast, the fluorescence at the top of the stem, farther from the roots, remained relatively stable. With the transportation of Cu^{2+}, the fluorescence changes at the top of the stem became noticeable. After 55 min, the fluorescence quenching was uniformly observed across the entire stem, with a total decrease of approximately 55%. As a control, no reduction in fluorescence was observed when nurturing in deionized water (Figure S27). These observations further validate that the (7,5) sensor is an effective and reliable tool for detecting and tracking the transport and distribution of Cu^{2+} ions within diverse plant tissues, thereby providing valuable insights into the dynamics of metal ion transport in plants.

Spinach (*Spinacia oleracea*), a commonly consumed leafy vegetable in daily diets, is particularly rich in copper due to its high capacity to absorb Cu^{2+} ions. We selected spinach as a model plant to examine the uptake and distribution of Cu^{2+} within the leaves. The (7,5) sensors were introduced into the spinach leaves via a nondestructive vacuum injection. NIR imaging of (7,5) distributed within the leaves exhibited an intense fluorescence signal (Figure S28). This signal remained stable with minimal fluctuation for a period of 5 h when the spinach was grown in water, manifesting the high stability of nanosensors within the plant's complex matrix. Subsequently, a dilute Cu^{2+} solution was supplied to the roots of spinach plants. As transpiration took place, the Cu^{2+} ions were absorbed by the roots and eventually interacted with the nanosensors embedded in the leaves, leading to fluorescence quenching over time. Specifically, after 5 h, there was a significant decrease of ~60% in the average fluorescence intensity (Figures 6a and S28c). The quenching of the fluorescence intensity showed an inverse linear correlation with the Cu^{2+} uptake time (Figure 6b, orange line). As a comparison, we conducted real-time imaging of spinach leaves cultivated in a mixed solution containing 13 ions for 4 h, with a concentration of each ion at 10 μM. The fluorescence intensity remained relatively stable throughout the measurement period (Figure S29), in contrast to the fluorescence quenching observed when the plants were exposed to a Cu^{2+} solution. These findings further support the selective detection of Cu^{2+} in in living plants.

To quantify the accumulation of Cu^{2+} in the leaves, inductively coupled plasma mass spectrometry (ICP-MS) was employed to create a calibration curve. This curve enables the conversion of changes in sensor intensity into a

https://doi.org/10.1021/acsnano.5c08364
ACS Nano 2025, 19, 28743−28754

quantitative measurement of Cu^{2+} concentration variations. Before conducting this analysis, it was essential to eliminate the interference caused by naturally occurring Cu^{2+} present in spinach. By using the Cu^{2+} content in untreated spinach as a baseline, we can quantitatively assess the Cu^{2+} levels in the treated spinach samples. For example, fluorescence decreases of 7.2% and 60% corresponded to 0.02 and 0.33 ppm of Cu^{2+} levels, respectively, after treating the leaves with a 10 μM Cu^{2+} solution for 1 and 5 h. We fitted the Cu^{2+} levels in spinach measured by ICP with the uptake time, yielding a linear correlation, as shown in Figure 6b (green line). Combining this with the orange fitting line, we can establish a linear relationship between the fluorescence change and the accumulated Cu^{2+} levels in the leaves (Figure 6c), which is described by the following equation:

$$[Cu^{2+}, \text{ppm}] = -0.59\Delta F - 0.011$$

Here, the ΔF represents the $(I-I_0)/I_0$ ratio from the (7,5) sensors embedded in the leaves. The quantitative correlation demonstrates our method's reliability and accessibility as a viable alternative to complex ICP-MS procedures, which require field sampling, digestion, and extraction.

Finally, to showcase the superior performance of our nanosensors over nonpurified counterparts in real-time imaging applications, we injected (7,5) and unpurified CNT sensors into two separate regions of a spinach leaf lamina. This allowed for a direct comparison of their sensing capabilities (Figure 6d). During the initial 60 min, the fluorescence intensity in both regions remained stable, as the Cu^{2+} ions had not yet interacted with the sensors (Figure 6e,f). After this interval, the fluorescence intensity in the region treated with (7,5) sensors diminished considerably, indicating a high sensitivity to even low concentrations of absorbed Cu^{2+}. In contrast, only a slight change in fluorescence was observed in the region treated with the CNT dispersion until 240 min, reflecting the low sensitivity of unpurified sensors. Beyond 240 min, the fluorescence from both sensors was rapidly quenched due to the accumulation of Cu^{2+}. Nevertheless, the (7,5) sensors maintained a higher level of sensitivity compared with the CNT dispersion (Figure 6f). These findings highlight the ultrasensitive nature of our nanosensors, a critical attribute for advancing the development of sensors that utilize optical and wireless signals to monitor plant health status in real time.

CONCLUSIONS

In summary, we have successfully developed a high-performance framework for the real-time and quantitative detection of Cu^{2+} ions in plants using purified DNA-scCNT sensors. This framework operates by monitoring the fluorescence reduction of scCNTs induced by the Cu^{2+} ions. We confirmed that the fluorescence quenching mechanism is attributed to electron transfer from the scCNTs to Cu^{2+} ions. Unlike the prior unpurified counterparts, the purified sensors are distinguished by their monochirality CNTs, which are wrapped with periodically helical DNA. The uniformity in chirality type and the well-defined DNA wrapping structures confer significant advantages to the purified DNA-scCNT sensors, including exceptional sensitivity, selectivity, stability, and clearly elucidated sensing mechanisms. Our assay is anticipated to be a starting point for the development of next-generation nanosensors based on purified DNA-scCNTs. The diverse combination of distinct chiralities of CNTs with controlled DNA helical structures will facilitate a promising platform capable of detecting ions, small molecules, and biomacromolecules with both sensitivity and specificity. This holds significant potential for a wide range of applications, ranging from precision agriculture to healthcare and disease diagnosis.

METHODS

Fluorescence Detection of Cu^{2+} in Aqueous Solution. The fluorescence assay for Cu^{2+} detection was conducted as follows: a solution of $C_3GC_6GC_4$-(7,5) was prepared to a final concentration of 0.2 optical density (OD). Small volumes of concentrated Cu^{2+} solutions were gradually added into the (7,5) solution to make the final concentration of Cu^{2+} ranging from 10^{-12} M to 10^{-4} M. The PL spectra of the (7,5) solution were then recorded at these varying Cu^{2+} concentrations. The same procedure was applied to detect Cu^{2+} using other types of scCNTs. The Cu^{2+} ions used in this study were derived from $Cu(NO_3)_2$, unless otherwise stated.

In the selective assay, Cu^{2+} was replaced with other metal ions, and the PL spectra were measured under the same conditions. To assess the anti-interference capability of (7,5), Cu^{2+} detection was performed in the presence of various ions. A solution of (7,5) (OD = 0.2) was prepared, and then solutions of salts containing different metal ions (each at 10^{-6} M) were added, followed by the addition of an equal concentration of Cu^{2+}. The PL spectra of (7,5) were then recorded.

$C_3GC_6GC_4$-(7,5)-Based Sensing Platform for Cu^{2+} Detection in Plants. Bean seedlings were obtained by incubating the seeds in deionized water for up to 6 days. One-month-old spinach plants with intact root systems were purchased from a local agricultural market. To monitor the uptake of (7,5) in plant roots, bean seedlings were incubated in a (7,5) solution (OD = 0.5) and placed in an NIR imaging system equipped with an InGaAs camera. The plants were then subjected to real-time imaging for 2 h using excitation from a 750 nm laser (Figure S21). A 1000-nm long-band-pass filter was placed in front of the camera lens to eliminate the interference of chlorophyll, autofluorescence, and the reflected excitation beam. To observe real-time changes in Cu^{2+} concentration in plant roots, the (7,5) sensors were first introduced into the roots of bean seedlings. The root surfaces were then washed with deionized water to remove residual (7,5). Subsequently, the treated plants were incubated in a 10 μM Cu^{2+} solution, and the concentration variation of Cu^{2+} was monitored in real time.

To observe the transmission and distribution of Cu^{2+} in plants, the stems of bean seedlings were infiltrated with (7,5) using a fine needle syringe. The treated plants were then incubated in a 10 μM Cu^{2+} solution and monitored by an imaging system. Similarly, (7,5) sensors were infiltrated into the leaves of spinach via nondestructive vacuum injection. The leaves were then carefully washed with deionized water to remove any residual (7,5) from the surface. Afterward, the treated plants were cultured in deionized water for 1 h to stabilize the sensor in the leaves and then transferred to a 10 μM Cu^{2+} solution for imaging collection.

Fluorescence images in false color were obtained using ImageJ software, and the fluorescence intensity data for (7,5) were extracted with the same software. Specifically, the sensor response was determined from the NIR images by normalizing the (7,5) fluorescence to the corresponding baseline value before the introduction of Cu^{2+}. The changes in fluorescence

https://doi.org/10.1021/acsnano.5c08364
ACS Nano 2025, 19, 28743−28754

intensity were quantified by summing the total fluorescence within predefined regions of the plants. Specifically, the fluorescence intensities of the entire root in Figure 5c and the whole leaf in Figure 6a were measured. For the stem of a bean seedling in Figure 5e, the fluorescence intensity in the regions marked by the dashed boxes was calculated to quantify the fluorescence of both the top and bottom stems.

ASSOCIATED CONTENT

Supporting Information

The Supporting Information is available free of charge at https://pubs.acs.org/doi/10.1021/acsnano.5c08364.

Materials and Methods; Figures S1−S29; Tables S1 and S2; and Additional discussion (PDF)

AUTHOR INFORMATION

Corresponding Author

Zhiwei Lin − *South China Advanced Institute for Soft Matter Science and Technology, School of Emergent Soft Matter, South China University of Technology, Guangzhou 510640, China; Guangdong Provincial Key Laboratory of Functional and Intelligent Hybrid Materials and Devices and Guangdong Basic Research Center of Excellence for Energy and Information Polymer Materials, South China University of Technology, Guangzhou 510640, China;* orcid.org/0000-0001-9194-1145; Email: zhiweilin@scut.edu.cn

Authors

Jianying Chen − *South China Advanced Institute for Soft Matter Science and Technology, School of Emergent Soft Matter, South China University of Technology, Guangzhou 510640, China*

Yinong Li − *South China Advanced Institute for Soft Matter Science and Technology, School of Emergent Soft Matter, South China University of Technology, Guangzhou 510640, China*

Jiajie Wu − *South China Advanced Institute for Soft Matter Science and Technology, School of Emergent Soft Matter, South China University of Technology, Guangzhou 510640, China*

Jialong Liu − *South China Advanced Institute for Soft Matter Science and Technology, School of Emergent Soft Matter, South China University of Technology, Guangzhou 510640, China*

Xuan Zhou − *South China Advanced Institute for Soft Matter Science and Technology, School of Emergent Soft Matter, South China University of Technology, Guangzhou 510640, China*

Zelong Li − *South China Advanced Institute for Soft Matter Science and Technology, School of Emergent Soft Matter, South China University of Technology, Guangzhou 510640, China*

Kunpeng Tang − *State Key Laboratory of Optoelectronic Materials and Technologies, Guangdong Basic Research Center of Excellence for Functional Molecular Engineering, Nanotechnology Research Center, School of Materials Science and Engineering, Sun Yat-sen University, Guangzhou 510275, China*

Lei Shi − *State Key Laboratory of Optoelectronic Materials and Technologies, Guangdong Basic Research Center of Excellence for Functional Molecular Engineering, Nanotechnology Research Center, School of Materials Science and Engineering, Sun Yat-sen University, Guangzhou 510275, China;* orcid.org/0000-0003-4175-7803

Zhilong Zhang − *South China Advanced Institute for Soft Matter Science and Technology, School of Emergent Soft Matter, South China University of Technology, Guangzhou 510640, China; Guangdong Provincial Key Laboratory of Functional and Intelligent Hybrid Materials and Devices, South China University of Technology, Guangzhou 510640, China;* orcid.org/0000-0001-9903-4945

Complete contact information is available at: https://pubs.acs.org/10.1021/acsnano.5c08364

Notes

The authors declare no competing financial interest.

ACKNOWLEDGMENTS

Z.L. acknowledges support from the National Key Research and Development Program of China (No. 2023YFA0915200), the National Natural Science Foundation of China (NSFC No. 52273265), the Guangdong Basic and Applied Basic Research Foundation (No. 2024A1515012437, 2024B1515040023), the R&D Program of Guangzhou (No. 2025A04J7015), the GJYC Program of Guangzhou (No. 2024D03J0002, 2024D01J0057), and the Xiaomi Foundation. Z.Z. acknowledges support from Guangdong Province (2025A1515010298) and Guangzhou City (SL2023A04J00824).

REFERENCES

(1) Binesh, A.; Venkatachalam, K. Copper in Human Health and Disease: A Comprehensive Review. *J. Biochem. Mol. Toxicol.* **2024**, *38* (11), No. e70052.

(2) Li, Z.; Ma, Z.; Van Der Kuijp, T. J.; Yuan, Z.; Huang, L. A Review of Soil Heavy Metal Pollution from Mines in China: Pollution and Health Risk Assessment. *Sci. Total Environ.* **2014**, *468−469*, 843−853.

(3) Abdelwaheb, M.; Nedeff, V.; Dridi-Dhaouadi, S.; Moşneguţu, E.; Barsan, N.; Chjimus, A.-D. Assessment of Cadmium and Copper Adsorption by Two Agricultural Soils from Romania and Tunisia: Risk of Water Resource Pollution. *Processes* **2022**, *10* (9), 1802.

(4) Fagnano, M.; Agrelli, D.; Pascale, A.; Adamo, P.; Fiorentino, N.; Rocco, C.; Pepe, O.; Ventorino, V. Copper Accumulation in Agricultural Soils: Risks for the Food Chain and Soil Microbial Populations. *Sci. Total Environ.* **2020**, *734*, 139434.

(5) Bandmann, O.; Weiss, K. H.; Kaler, S. G. Wilson's Disease and Other Neurological Copper Disorders. *Lancet Neurol.* **2015**, *14* (1), 103−113.

(6) Li, Y.; Yang, C.; Wang, S.; Yang, D.; Zhang, Y.; Xu, L.; Ma, L.; Zheng, J.; Petersen, R. B.; Zheng, L.; Chen, H.; Huang, K. Copper and Iron Ions Accelerate the Prion-like Propagation of α-Synuclein: A Vicious Cycle in Parkinson's Disease. *Int. J. Biol. Macromol.* **2020**, *163*, 562−573.

(7) Bost, M.; Houdart, S.; Oberli, M.; Kalonji, E.; Huneau, J.-F.; Margaritis, I. Dietary Copper and Human Health: Current Evidence and Unresolved Issues. *J. Trace Elem. Med. Biol.* **2016**, *35*, 107−115.

(8) Kriegeskotte, C.; Cantz, T.; Haberland, J.; Zibert, A.; Haier, J.; Köhler, G.; Schöler, H. R.; Schmidt, H. H.-J.; Arlinghaus, H. F. Laser Secondary Neutral Mass Spectrometry for Copper Detection in Micro-scale Biopsies. *J. Mass Spectrom.* **2009**, *44* (10), 1417−1422.

(9) Lew, T. T. S.; Park, M.; Cui, J.; Strano, M. S. Plant Nanobionic Sensors for Arsenic Detection. *Adv. Mater.* **2021**, *33* (1), 2005683.

(10) Wulf, V.; Bichachi, E.; Hendler-Neumark, A.; Massarano, T.; Leshem, A. B.; Lampel, A.; Bisker, G. Multicomponent System of Single-Walled Carbon Nanotubes Functionalized with a Melanin-Inspired Material for Optical Detection and Scavenging of Metals. *Adv. Funct. Mater.* **2022**, *32* (49), 2209688.

(11) O'Connell, M. J.; Bachilo, S. M.; Huffman, C. B.; Moore, V. C.; Strano, M. S.; Haroz, E. H.; Rialon, K. L.; Boul, P. J.; Noon, W. H.; Kittrell, C.; Ma, J.; Hauge, R. H.; Weisman, R. B.; Smalley, R. E. Band Gap Fluorescence from Individual Single-Walled Carbon Nanotubes. *Science* **2002**, *297* (5581), 593−596.
(12) Ackermann, J.; Metternich, J. T.; Herbertz, S.; Kruss, S. Biosensing with Fluorescent Carbon Nanotubes. *Angew. Chem., Int. Ed.* **2022**, *61* (18), No. e202112372.
(13) Settele, S.; Schrage, C. A.; Jung, S.; Michel, E.; Li, H.; Flavel, B. S.; Hashmi, A. S. K.; Kruss, S.; Zaumseil, J. Ratiometric fluorescent sensing of pyrophosphate with sp^3-functionalized single-walled carbon nanotubes. *Nat. Commun.* **2024**, *15* (1), 706.
(14) Kruss, S.; Landry, M. P.; Vander Ende, E.; Lima, B. M. A.; Reuel, N. F.; Zhang, J.; Nelson, J.; Mu, B.; Hilmer, A.; Strano, M. Neurotransmitter Detection Using Corona Phase Molecular Recognition on Fluorescent Single-Walled Carbon Nanotube Sensors. *J. Am. Chem. Soc.* **2014**, *136* (2), 713−724.
(15) Beyene, A. G.; Delevich, K.; Bonis-O'Donnell, J. T. D.; Piekarski, D. J.; Lin, W. C.; Thomas, A. W.; Yang, S. J.; Kosillo, P.; Yang, D.; Prounis, G. S.; et al. Imaging Striatal Dopamine Release Using a Nongenetically Encoded near Infrared Fluorescent Catecholamine Nanosensor. *Sci. Adv.* **2019**, *5*, No. eaaw3108.
(16) Kruss, S.; Salem, D. P.; Vuković, L.; Lima, B.; Vander Ende, E.; Boyden, E. S.; Strano, M. S. High-Resolution Imaging of Cellular Dopamine Efflux Using a Fluorescent Nanosensor Array. *Proc. Natl. Acad. Sci. U. S. A.* **2017**, *114* (8), 1789−1794.
(17) Giraldo, J. P.; Landry, M. P.; Faltermeier, S. M.; McNicholas, T. P.; Iverson, N. M.; Boghossian, A. A.; Reuel, N. F.; Hilmer, A. J.; Sen, F.; Brew, J. A.; Strano, M. S. Plant Nanobionics Approach to Augment Photosynthesis and Biochemical Sensing. *Nat. Mater.* **2014**, *13* (4), 400−408.
(18) Zheng, M.; Jagota, A.; Semke, E. D.; Diner, B. A.; Mclean, R. S.; Lustig, S. R.; Richardson, R. E.; Tassi, N. G. DNA-Assisted Dispersion and Separation of Carbon Nanotubes. *Nat. Mater.* **2003**, *2* (5), 338−342.
(19) Heller, D. A.; Baik, S.; Eurell, T. E.; Strano, M. S. Single-Walled Carbon Nanotube Spectroscopy in Live Cells: Towards Long-Term Labels and Optical Sensors. *Adv. Mater.* **2005**, *17* (23), 2793−2799.
(20) Pinals, R. L.; Ledesma, F.; Yang, D.; Navarro, N.; Jeong, S.; Pak, J. E.; Kuo, L.; Chuang, Y.-C.; Cheng, Y.-W.; Sun, H.-Y.; Landry, M. P. Rapid SARS-CoV-2 Spike Protein Detection by Carbon Nanotube-Based Near-Infrared Nanosensors. *Nano Lett.* **2021**, *21* (5), 2272−2280.
(21) Kim, M.; Chen, C.; Wang, P.; Mulvey, J. J.; Yang, Y.; Wun, C.; Antman-Passig, M.; Luo, H.-B.; Cho, S.; Long-Roche, K.; Ramanathan, L. V.; Jagota, A.; Zheng, M.; Wang, Y.; Heller, D. A. Detection of Ovarian Cancer via the Spectral Fingerprinting of Quantum-Defect-Modified Carbon Nanotubes in Serum by Machine Learning. *Nat. Biomed. Eng.* **2022**, *6* (3), 267−275.
(22) Williams, R. M.; Lee, C.; Heller, D. A. A Fluorescent Carbon Nanotube Sensor Detects the Metastatic Prostate Cancer Biomarker uPA. *ACS Sens.* **2018**, *3* (9), 1838−1845.
(23) Nißler, R.; Müller, A. T.; Dohrman, F.; Kurth, L.; Li, H.; Cosio, E. G.; Flavel, B. S.; Giraldo, J. P.; Mithöfer, A.; Kruss, S. Detection and Imaging of the Plant Pathogen Response by Near-Infrared Fluorescent Polyphenol Sensors. *Angew. Chem., Int. Ed.* **2022**, *61* (2), No. e202108373.
(24) Landry, M. P.; Ando, H.; Chen, A. Y.; Cao, J.; Kottadiel, V. I.; Chio, L.; Yang, D.; Dong, J.; Lu, T. K.; Strano, M. S. Single-Molecule Detection of Protein Efflux from Microorganisms Using Fluorescent Single-Walled Carbon Nanotube Sensor Arrays. *Nat. Nanotechnol.* **2017**, *12* (4), 368−377.
(25) Zheng, Y.; Bachilo, S. M.; Weisman, R. B. Quenching of Single-Walled Carbon Nanotube Fluorescence by Dissolved Oxygen Reveals Selective Single-Stranded DNA Affinities. *J. Phys. Chem. Lett.* **2017**, *8* (9), 1952−1955.
(26) Xhyliu, F.; Ao, G. Chirality-Pure Carbon Nanotubes Show Distinct Complexation with Recognition DNA Sequences. *Carbon* **2020**, *167*, 601−608.
(27) Krasley, A. T.; Chakraborty, S.; Vuković, L.; Beyene, A. G. Molecular Determinants of Optical Modulation in ssDNA−Carbon Nanotube Biosensors. *ACS Nano* **2025**, *19* (8), 7804−7820.
(28) Basu, S.; Hendler-Neumark, A.; Bisker, G. Role of Oxygen Defects in Eliciting a Divergent Fluorescence Response of Single-Walled Carbon Nanotubes to Dopamine and Serotonin. *ACS Nano* **2024**, *18* (50), 34134−34146.
(29) Kelich, P.; Jeong, S.; Navarro, N.; Adams, J.; Sun, X.; Zhao, H.; Landry, M. P.; Vuković, L. Discovery of DNA−Carbon Nanotube Sensors for Serotonin with Machine Learning and Near-Infrared Fluorescence Spectroscopy. *ACS Nano* **2022**, *16* (1), 736−745.
(30) Yaari, Z.; Yang, Y.; Apfelbaum, E.; Cupo, C.; Settle, A. H.; Cullen, Q.; Cai, W.; Roche, K. L.; Levine, D. A.; Fleisher, M.; et al. A Perception-Based Nanosensor Platform to Detect Cancer Biomarkers. *Sci. Adv.* **2021**, *7* (47), No. eabj0852.
(31) Ao, G.; Khripin, C. Y.; Zheng, M. DNA-Controlled Partition of Carbon Nanotubes in Polymer Aqueous Two-Phase Systems. *J. Am. Chem. Soc.* **2014**, *136* (29), 10383−10392.
(32) Ao, G.; Streit, J. K.; Fagan, J. A.; Zheng, M. Differentiating Left- and Right-Handed Carbon Nanotubes by DNA. *J. Am. Chem. Soc.* **2016**, *138* (51), 16677−16685.
(33) Lin, Z.; Yang, Y.; Jagota, A.; Zheng, M. Machine Learning-Guided Systematic Search of DNA Sequences for Sorting Carbon Nanotubes. *ACS Nano* **2022**, *16* (3), 4705−4713.
(34) Zhou, X.; Wang, P.; Li, Y.; Han, Y.; Chen, J.; Tang, K.; Shi, L.; Zhang, Y.; Zhang, R.; Lin, Z. Accurate DNA Sequence Prediction for Sorting Target-Chirality Carbon Nanotubes and Manipulating Their Functionalities. *ACS Nano* **2025**, *19* (2), 2665−2676.
(35) Tu, X.; Manohar, S.; Jagota, A.; Zheng, M. DNA Sequence Motifs for Structure-Specific Recognition and Separation of Carbon Nanotubes. *Nature* **2009**, *460* (7252), 250−253.
(36) Lyu, M.; Meany, B.; Yang, J.; Li, Y.; Zheng, M. Toward Complete Resolution of DNA/Carbon Nanotube Hybrids by Aqueous Two-Phase Systems. *J. Am. Chem. Soc.* **2019**, *141* (51), 20177−20186.
(37) Wu, X.; Kim, M.; Wang, L. J.; Veetil, A. K.; Wang, Y. Programming Sp^3 Quantum Defects along Carbon Nanotubes with Halogenated DNA. *J. Am. Chem. Soc.* **2024**, *146* (13), 8826−8831.
(38) Nißler, R.; Ackermann, J.; Ma, C.; Kruss, S. Prospects of Fluorescent Single-Chirality Carbon Nanotube-Based Biosensors. *Anal. Chem.* **2022**, *94* (28), 9941−9951.
(39) Nißler, R.; Kurth, L.; Li, H.; Spreinat, A.; Kuhlemann, I.; Flavel, B. S.; Kruss, S. Sensing with Chirality-Pure Near-Infrared Fluorescent Carbon Nanotubes. *Anal. Chem.* **2021**, *93* (16), 6446−6455.
(40) Ackermann, J.; Stegemann, J.; Smola, T.; Reger, E.; Jung, S.; Schmitz, A.; Herbertz, S.; Erpenbeck, L.; Seidl, K.; Kruss, S. High Sensitivity Near-Infrared Imaging of Fluorescent Nanosensors. *Small* **2023**, *19* (14), 2206856.
(41) Li, Y.; Wen, Y.; Beltrán, L. C.; Zhu, L.; Tian, S.; Liu, J.; Zhou, X.; Chen, P.; Egelman, E. H.; Zheng, M.; et al. Understanding DNA-Encoded Carbon Nanotube Sorting and Sensing via Sub-nm-Resolution Structural Determination. *Sci. Adv.* **2025**, *11* (14), No. eadt9844.
(42) Brege, J. J.; Gallaway, C.; Barron, A. R. Fluorescence Quenching of Single-Walled Carbon Nanotubes with Transition-Metal Ions. *J. Phys. Chem. C* **2009**, *113* (11), 4270−4276.
(43) Settele, S.; Stammer, F.; Sebastian, F. L.; Lindenthal, S.; Wald, S. R.; Li, H.; Flavel, B. S.; Zaumseil, J. Easy Access to Bright Oxygen Defects in Biocompatible Single-Walled Carbon Nanotubes via a Fenton-like Reaction. *ACS Nano* **2024**, *18* (31), 20667−20678.
(44) Santos, S. M.; Yuma, B.; Berciaud, S.; Shaver, J.; Gallart, M.; Gilliot, P.; Cognet, L.; Lounis, B. All-Optical Trion Generation in Single-Walled Carbon Nanotubes. *Phys. Rev. Lett.* **2011**, *107* (18), 187401.
(45) Hackl, E. V.; Kornilova, S. V.; Blagoi, Y. P. DNA Structural Transitions Induced by Divalent Metal Ions in Aqueous Solutions. *Int. J. Biol. Macromol.* **2005**, *35* (3−4), 175−191.

https://doi.org/10.1021/acsnano.5c08364
ACS Nano 2025, 19, 28743−28754

(46) Zhou, M.; Xu, T.; Xia, K.; Gao, H.; Li, W.; Zhai, T.; Gu, H. Small DNAs That Specifically and Tightly Bind Transition Metal Ions. *J. Am. Chem. Soc.* **2023**, *145* (16), 8776−8780.
(47) Kopicki, J.-D.; Saikia, A.; Niebling, S.; Günther, C.; Anjanappa, R.; Garcia-Alai, M.; Springer, S.; Uetrecht, C. Opening Opportunities for Kd Determination and Screening of MHC Peptide Complexes. *Commun. Biol.* **2022**, *5* (1), 488.
(48) Zhang, H.; Feng, L.; Jiang, Y.; Wong, Y.-T.; He, Y.; Zheng, G.; He, J.; Tan, Y.; Sun, H.; Ho, D. A Reaction-Based Near-Infrared Fluorescent Sensor for Cu^{2+} Detection in Aqueous Buffer and Its Application in Living Cells and Tissues Imaging. *Biosens. Bioelectron.* **2017**, *94*, 24−29.
(49) Sauzéat, L.; Costas-Rodríguez, M.; Albalat, E.; Mattielli, N.; Vanhaecke, F.; Balter, V. Inter-Comparison of Stable Iron, Copper and Zinc Isotopic Compositions in Six Reference Materials of Biological Origin. *Talanta* **2021**, *221*, 121576.
(50) Lin, J.; Huang, X.; Kou, E.; Cai, W.; Zhang, H.; Zhang, X.; Liu, Y.; Li, W.; Zheng, Y.; Lei, B. Carbon Dot Based Sensing Platform for Real-Time Imaging Cu^{2+} Distribution in Plants and Environment. *Biosens. Bioelectron.* **2023**, *219*, 114848.
(51) Andrushchenko, V.; Van De Sande, J. H.; Wieser, H. Vibrational Circular Dichroism and IR Absorption of DNA Complexes with Cu^{2+} Ions. *Biopolymers* **2003**, *72* (5), 374−390.
(52) Streit, J. K.; Fagan, J. A.; Zheng, M. A Low Energy Route to DNA-Wrapped Carbon Nanotubes via Replacement of Bile Salt Surfactants. *Anal. Chem.* **2017**, *89* (19), 10496−10503.
(53) Bissett, M. A.; Konabe, S.; Okada, S.; Tsuji, M.; Ago, H. Enhanced Chemical Reactivity of Graphene Induced by Mechanical Strain. *ACS Nano* **2013**, *7* (11), 10335−10343.
(54) Che, T.; Liu, S.; Wang, Y.; Zhao, P.; Yang, C.; Pan, X.; Ji, H.; Geng, L.; Sun, Q.; Hu, Z.; Li, A.; Zhou, C.; Xu, L.-C.; Zhong, Y.; Tian, D.; Yang, Y.; Kang, L. Interfacial Charge Transfer in One-Dimensional AgBr Encapsulated inside Single-Walled Carbon Nanotube Heterostructures. *ACS Nano* **2024**, *18* (47), 32569−32577.
(55) Cui, K.; Qian, Y.; Jeon, I.; Anisimov, A.; Matsuo, Y.; Kauppinen, E. I.; Maruyama, S. Scalable and Solid-State Redox Functionalization of Transparent Single-Walled Carbon Nanotube Films for Highly Efficient and Stable Solar Cells. *Adv. Energy Mater.* **2017**, *7* (18), 1700449.
(56) Dresselhaus, M. S.; Jorio, A.; Hofmann, M.; Dresselhaus, G.; Saito, R. Perspectives on Carbon Nanotubes and Graphene Raman Spectroscopy. *Nano Lett.* **2010**, *10* (3), 751−758.
(57) Maciel, I. O.; Campos-Delgado, J.; Cruz-Silva, E.; Pimenta, M. A.; Sumpter, B. G.; Meunier, V.; López-Urías, F.; Muñoz-Sandoval, E.; Terrones, H.; Terrones, M.; Jorio, A. S. Electronic Structure, and Raman Scattering of Phosphorus-Doped Single-Wall Carbon Nanotubes. *Nano Lett.* **2009**, *9* (6), 2267−2272.
(58) Maciel, I. O.; Anderson, N.; Pimenta, M. A.; Hartschuh, A.; Qian, H.; Terrones, M.; Terrones, H.; Campos-Delgado, J.; Rao, A. M.; Novotny, L.; Jorio, A. Electron and Phonon Renormalization Near Charged Defects in Carbon Nanotubes. *Nat. Mater.* **2008**, *7* (11), 878−883.
(59) Li, Y.; Zhang, Y.; Hou, R.; Ai, Y.; Cai, M.; Shi, Z.; Zhang, P.; Shao, G. Revealing Electron Numbers-Binding Energy Relationships in Heterojunctions via in-Situ Irradiated XPS. *Appl. Catal. B Environ. Energy* **2024**, *356*, 124223.
(60) Sun, Q.-M.; Xu, J.-J.; Tao, F.-F.; Ye, W.; Zhou, C.; He, J.-H.; Lu, J.-M. Boosted Inner Surface Charge Transfer in Perovskite Nanodots@Mesoporous Titania Frameworks for Efficient and Selective Photocatalytic CO_2 Reduction to Methane. *Angew. Chem., Int. Ed.* **2022**, *61* (20), No. e202200872.
(61) Liu, P.; Hensen, E. J. M. Highly Efficient and Robust Au/$MgCuCr_2O_4$ Catalyst for Gas-Phase Oxidation of Ethanol to Acetaldehyde. *J. Am. Chem. Soc.* **2013**, *135* (38), 14032−14035.
(62) Pang, J.; Zheng, M.; Wang, C.; Yang, X.; Liu, H.; Liu, X.; Sun, J.; Wang, Y.; Zhang, T. Hierarchical Echinus-like Cu-MFI Catalysts for Ethanol Dehydrogenation. *ACS Catal.* **2020**, *10* (22), 13624−13629.
(63) Zheng, M.; Diner, B. A. Solution Redox Chemistry of Carbon Nanotubes. *J. Am. Chem. Soc.* **2004**, *126* (47), 15490−15494.
(64) O'Connell, M. J.; Eibergen, E. E.; Doorn, S. K. Chiral Selectivity in the Charge-Transfer Bleaching of Single-Walled Carbon-Nanotube Spectra. *Nat. Mater.* **2005**, *4* (5), 412−418.
(65) Satishkumar, B. C.; Brown, L. O.; Gao, Y.; Wang, C.-C.; Wang, H.-L.; Doorn, S. K. Reversible Fluorescence Quenching in Carbon Nanotubes for Biomolecular Sensing. *Nat. Nanotechnol.* **2007**, *2* (9), 560−564.
(66) Ruckebusch, C.; Sliwa, M.; Pernot, P.; De Juan, A.; Tauler, R. Comprehensive Data Analysis of Femtosecond Transient Absorption Spectra: A Review. *J. Photochem. Photobiol., C* **2012**, *13* (1), 1−27.
(67) Menon, A.; Slominskii, Y. L.; Joseph, J.; Dimitriev, O. P.; Guldi, D. M. Reversible Charge Transfer with Single-Walled Carbon Nanotubes Upon Harvesting the Low Energy Part of the Solar Spectrum. *Small* **2020**, *16* (8), 1906745.
(68) Zhang, J.; Yang, G.; He, B.; Cheng, B.; Li, Y.; Liang, G.; Wang, L. Electron Transfer Kinetics in CdS/Pt Heterojunction Photocatalyst during Water Splitting. *Chin. J. Catal.* **2022**, *43* (10), 2530−2538.
(69) Chmeliov, J.; Narkeliunas, J.; Graham, M. W.; Fleming, G. R.; Valkunas, L. Exciton−Exciton Annihilation and Relaxation Pathways in Semiconducting Carbon Nanotubes. *Nanoscale* **2016**, *8* (3), 1618−1626.
(70) Ma, Y.-Z.; Valkunas, L.; Dexheimer, S. L.; Bachilo, S. M.; Fleming, G. R. Femtosecond Spectroscopy of Optical Excitations in Single-Walled Carbon Nanotubes: Evidence for Exciton-Exciton Annihilation. *Phys. Rev. Lett.* **2005**, *94* (15), 157402.
(71) Tumiel, T. M.; Amin, M.; Krauss, T. D. Single-Walled Carbon Nanotube Dark Exciton Photoluminescence Dynamics. *J. Phys. Chem. C* **2021**, *125* (45), 25022−25029.
(72) Isokuortti, J.; Kuntze, K.; Virkki, M.; Ahmed, Z.; Vuorimaa-Laukkanen, E.; Filatov, M. A.; Turshatov, A.; Laaksonen, T.; Priimagi, A.; Durandin, N. A. Expanding Excitation Wavelengths for Azobenzene Photoswitching into the Near-Infrared Range *via* Endothermic Triplet Energy Transfer. *Chem. Sci.* **2021**, *12* (21), 7504−7509.
(73) Wang, C.; Wegeberg, C.; Wenger, O. S. First-Row D6Metal Complex Enables Photon Upconversion and Initiates Blue Light-Dependent Polymerization with Red Light. *Angew. Chem., Int. Ed.* **2023**, *62* (43), No. e202311470.
(74) Khodakovskaya, M. V.; Kim, B.-S.; Kim, J. N.; Alimohammadi, M.; Dervishi, E.; Mustafa, T.; Cernigla, C. E. Carbon Nanotubes as Plant Growth Regulators: Effects on Tomato Growth, Reproductive System, and Soil Microbial Community. *Small* **2013**, *9* (1), 115−123.
(75) Mathew, S.; Tiwari, D. K.; Tripathi, D. Interaction of Carbon Nanotubes with Plant System: A Review. *Carbon Lett.* **2021**, *31* (2), 167−176.
(76) Kumar, V.; Pandita, S.; Singh Sidhu, G. P.; Sharma, A.; Khanna, K.; Kaur, P.; Bali, A. S.; Setia, R. Copper bioavailability, uptake, toxicity and tolerance in plants: A comprehensive review. *Chemosphere* **2021**, *262*, 127810.

https://doi.org/10.1021/acsnano.5c08364
ACS Nano 2025, 19, 28743−28754